HTML ABSTRACT + LINKS

JOURNAL OF APPLIED PHYSICS VOLUME 96, NUMBER 7 1 OCTOBER 2004

Evolution of dislocation structure in the heat affected zone of a nickel-based single crystal

O. M. Barabash,[a] J. A. Horton, S. S. Babu, J. M. Vitek, S. A. David, J. W. Park, G. E. Ice, and R. I. Barabash
Metals & Ceramics Division, Oak Ridge National Laboratory, Oak Ridge, Tennessee 37831

(Received 10 February 2004; accepted 9 June 2004)

Using polychromatic microbeam synchrotron diffraction together with electron and optical microscopy, we studied dislocation structure changes of Ni—based single crystal superalloy during impulse heating up to the melting temperature. It is shown that the distribution of the thermal gradient is not monotonic. The maximum value of the thermal gradient is observed in the heat affected zone near the fusion line. Depending on the temperature, the formation of dislocation is accompanied by the partial or complete dissolution of γ' particles in the matrix. Dislocations form and multiply due to thermal gradients, and their arrangement correlates with temperature gradient field and with the dissolution and reprecipitation of γ' particles. © *2004 American Institute of Physics*. [DOI: 10.1063/1.1777393]

I. INTRODUCTION

The heat affected zone (HAZ) that forms during welding of different materials is in the immediate vicinity of the fusion zone and forms as a result of heating to below the melting temperature and subsequent cooling. The HAZ is an important part of the weld and determines many of the weld properities. The HAZ which is formed during welding of a single crystal nickel-based alloy has some specific features[1–3] as a consequence of the absence of grain boundaries and the presence of strengthening γ' phase particles with the volume fractions up to 75% after preliminary heat treatment. Formations of this zone is accompanied by the full or partial dissolution of γ' particles in the γ' matrix and their reprecipitaiton from the solid solution during cooling because during spot welding the local temperature near the fusion line (FL) exceeds the solvus temperature for this alloy. As a result, the γ' phase particle size and distribution change and a bimodal distribution are formed with large primary particles and secondary γ' particles an order of magnitude smaller in size.

Due to the thermal cycling during welding of nickel-based single crystals, dissolution and reprecipitation of γ' phase particles takes place simultaneously with thermal expansion contraction, resulting in strong plastic deformation in the HAZ and the whole weld.[1,2] This is one of the main problems during welding. The present paper describes an analysis of structure changes including dislocation formation in the HAZ during welding of nickel-based single crystals.

II. EXPREIMENTAL PROCEDURE

We have analyzed the structure of the HAZ, formed during spot welding of a TSM 75 nickel-based single crystal. The composition of the alloy is (wt%): Co-12.0; Cr-2.94; Mc-1.97; W-6.0; Ta-6.05; Al-6.06; Re-5.01; Hf-0.11; C-.0042; and balance nickel. The welding experiments were carried out on the end of a single crystal rod that was 60 mm long and 13 mm in diameter. The initial single crystal had a dendrite microstructure as a result of its original casting. Dendrites were oriented along the [001] sample axis (±2.5°). Spot welds were made on the rod using a gas tungsten are process, on the plane perpendicular to the [001] axis. This direction coincides with the growth directions of dendrites in fcc materials. Such orientation of the sample was chosen to force dendrites to grow in the direction of the temperature gradient along the sample axis. The arc was on for 17 s and then it was switched off immediately so that the samples were rapidly cooled. Cooling rate during this process was several orders of magnitude higher than during casting of the initial single crystals.

We analyzed two types of samples (Fig. 1): (1) samples

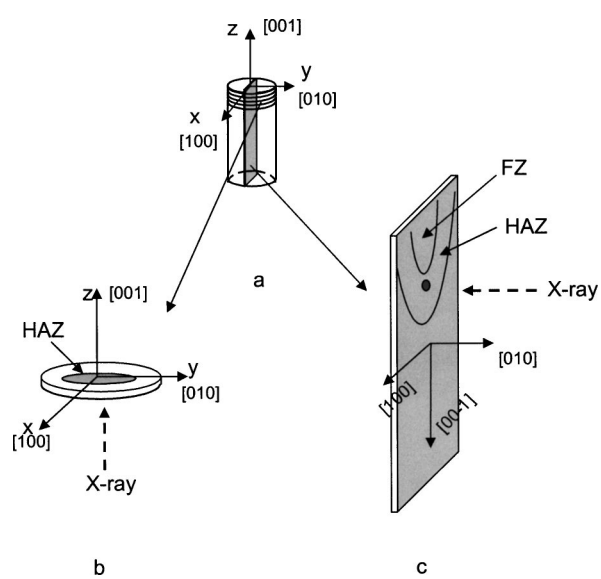

FIG. 1. (a) Scheme of the sample orientation relative to the cylinder axes of the single crystal: (b) Sample for Laue diffraction and TEM; (c) Sample for synchrotron microbeam Laue diffraction. Dot indicates the positions at which the diffraction pattern was obtained.

[a]Author to whom correspondence should be addressed; electronic mail: barabashom@ornl.gov

 © 2004 American Institute of Physics

Downloaded 04 Sep 2009 to 160.91.157.167. Redistribution subject to AIP license or copyright; see http://jap.aip.org/jap/copyright.jsp

of the first type were prepared as disks with a thickness of 0.3 mm, obtained by cutting the cylinder samples parallel to the (001) surface plane; (2) samples of the second type were prepared by cutting the samples along their [001] axis parallel to the (010) plane. The former samples were used for TEM and Laue diffraction while the latter were used for x-ray synchrotron measurements. All samples were bulk polished electrolytically to remove surface damage. The structures of all samples were analyzed by optical microscopy and Laue diffraction as well. The beam diameter for conventional Laue diffraction experiments was ≈0.4 mm. The x-ray synchrotron measurements were made with a three-dimensional (3D) x-ray crystal microscope, using a modified Laue diffraction method based on polychromatic radiation.[4,5] This approach allows for true 3D mapping of the crystalline phase, orientation, and plastic deformation with 1 μm spatial resolution. A region of interest is identified using an optical microscope and the polychromatic x-ray beam is then focused onto the sample. The orientation at each position of the crystal is precisely determined by an automated indexing program. Details on the experimental step and data collection can be found elsewhere.[4] Data were collected using microbeam Laue diffraction on the 34ID beamline at the Advanced Photon Source. Dimensions of the beam were 0.5×0.5 μm with a penetration depth of ~30 μm. The Laue diffraction and Synchrotron diffraction were done with white beams; therefore γ and γ' phases could not be distinguished.

Samples were also analyzed with TEM, using a Philips-CM30 transmission electron microscope. Samples for TEM were electropolished at a voltage of 9 V in an electrolyte containing 45% sulphuric acid and methanol.

III. RESULTS

A. Modeling of thermal parameters in the HAZ

The structure state in the HAZ depends on the thermal history of the process including the distribution of temperature, its gradient and rate of cooling.

The spot welding process was simulated with the finite element method using ABAQUS®.[6] To simplify the calculations the rod-shaped specimen was modeled as a cylindrical, axisymmetric specimen of 6.5 mm radius and 60 mm height. Eight node quadratic, rectangular elements were used in a mesh. The left boundary of the mesh was the edge of symmetry. The mesh was refined closer to the top surface and near the edge of symmetry since the largest temperature gradients occur in these regions.

The Gaussian heat source function by Goldak[7] was used. Temperature dependent material properties were used and heat loss on the surface by convection and radiation was considered. The thermal modeling results were calibrated by weld-cross section shape fitting.[1]

A section of the weld is shown in Fig. 2(a) and the thermal modeling results of the temperature distribution, its gradient, and its second derivative along the cylindrical axis of the sample after heating for 17 s and switching off the arc are shown in the Fig. 2(b). The temperature change with time and the rate of cooling of a point P_1 located in the HAZ at the distance 0.05 mm from the (FL) are shown at Fig. 2(a). For the analysis of the results we used the temperature dependence of the mole percent of γ' phase in the matrix of the TSM75 alloy as calculated using Thermo Calc[8] and the Ni-Data database[9] [Fig. 2(d)]. Analysis of these results shows that within the HAZ, the maximum temperature change, its gradient, and rate of cooling are localized in a small region very close to the FL.

In this region we expect the most important changes in the microstructure. The size of the HAZ depends on the welding condition. In our experiments the size of this zone, as determined by the etching pattern, is ~280 μm [Fig. 2(a)]. The FL corresponds to the solidus temperature of the analyzed alloy, ~1625 K. Using the calculated temperature distribution along the sample axis and the experimental size of the HAZ (280 μm), we estimate the temperature corresponding to the lower temperature limit of the HAZ as 1586 K [Fig. 2(a)]. This nearly coincides with the calculated γ' solvus temperature (1591 K) for the alloy.

B. X-ray analysis of the HAZ dislocation structure

In polychromatic diffraction, the incident and scattered beams each define a line in reciprocal space. The length of the line is determined by the wavelength of the radiation. Since white beam conditions are used, a continuous range of incident and scattered reciprocal space vector lengths are present. Furthermore, higher orders of reciprocal lattice points (for example, (00*h*), (002*h*), (003*h*), (004*h*) etc.) lie along the same directions and therefore will lead to scattering at the same pixel on the detector. Ordered $L1_2$ γ' phase particles are coherent with matrix and $[001]_{\gamma}\|[001]_{\text{matrix}}$, $(001)_{\gamma'}\|(001)_{\text{matrix}}$. That is why superlattice reflections from γ'phase overlap with structure reflections of the γ matrix. Figure 3 presents Laue patterns from the first sample type obtained from different positions in the weld joint. Laue patterns obtained from the FZ and from the base material (BM) (at a distance 10 mm from the FL) have sharp Laue spots [Figs. 3(a) and 3(b)]. This indicates a high degree of lattice perfection in these regions of the weld joint. Laue patterns obtained from the region located in the HAZ, ~100 μm from the FL, have a very different shape: each Laue spot is a streak [Fig. 3(c)]. The streaks are oriented in a specific way relative to the crystallographic axes of the single crystal. According to the method described in Ref. 5 an analysis of the crystallographic anisotropy of the Laue streaks and their full width at half maximum (FWHM) allows one to determine the density of unpaired dislocations and the activated and/or resulting slip systems. The total density of unpaired dislocations (n^+) in this region is $n^+=3.16\times10^8\text{cm}^{-2}$. The simulated Laue pattern [Fig. 3(d)] that best fits the experimental one [Fig. 3(c)] corresponds to the following main slip systems: Burgers vector $\mathbf{b}=[110]$, dislocation lines $\boldsymbol{\tau}_1=[1\bar{1}2]$, and $\boldsymbol{\tau}_2=[\bar{1}12]$; or $\mathbf{b}=[\bar{1}10]$, dislocation lines $\boldsymbol{\tau}_3=[112]$, and $\boldsymbol{\tau}_4=[11\bar{2}]$. Conventional Laue diffraction gives the average information (within the volume probed by the beam) about the direction of slip in the weld relative to the direction of the weld direction and thermal stresses at the structure level of 20–200 μm.

Downloaded 04 Sep 2009 to 160.91.157.167. Redistribution subject to AIP license or copyright; see http://jap.aip.org/jap/copyright.jsp

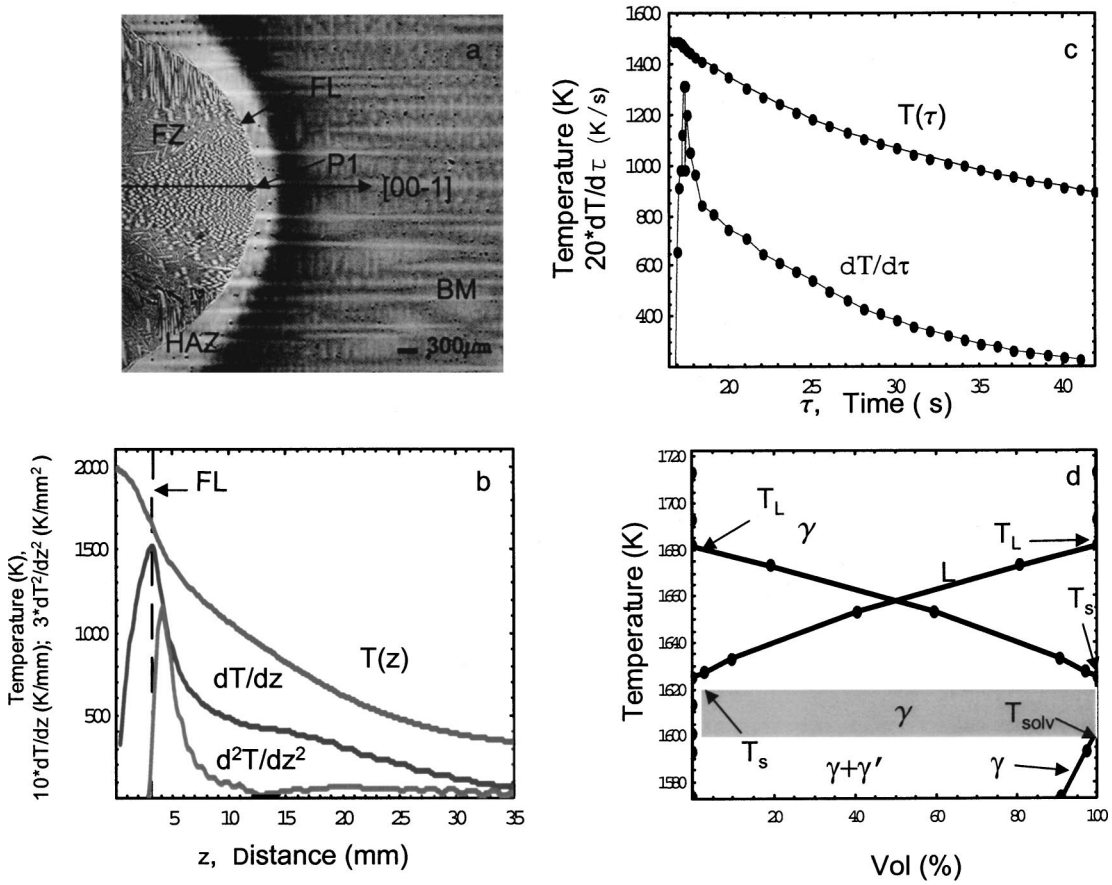

FIG. 2. Thermal-physical parameters of local melt for TSM-75 single cyrstal: (a) Micrograph of weld along the cylindrical axis; (b) Distributions of temperature, temperature gradient and its second derivative along the cylinder axis of the single crystal; (c) Temperature change with time and cooling rate in the point P_1 located near the FL; (d) Equilibrium transformation temperatures and temperature dependence of volume fraction of liquid and γ phase for TSM75 alloy.

The next "mesoscopic" level with the size of about (0.2–3) μm was analyzed for the second type of sample using synchrotron microbeam Laue diffraction. The Laue pattern from that sample is shown at Fig. 4(a). The location of the analyzed position in the HAZ is ~100 μm from FL. In contrast to conventional Laue diffraction, microbeam synchrotron measurements provide a very local information (within several microns) about the plastic activity in the HAZ, and follow the change in the activated slip systems in different zones of the HAZ. This Laue pattern also shows streaks, indicative of a specific dislocation system. The presence of streaking means that the crystallographic planes are rotated within the beam path having a submicron diameter. The length of the streaking is proportional to the number of unpaired dislocations and the direction of the streaking is sensitive to the line orientation of unpaired dislocations and their distribution in the grain. Streaking in an experimental Laue pattern [Fig. 4(a)] was modeled to identify the active slip system(s) at this location. Analysis of this Laue pattern shows that the streak orientation corresponds to a dislocation system with $\mathbf{b}=[110]$ and $\boldsymbol{\tau}=[21\bar{1}]$ [Fig. 4(b)]. Such a result coincides with the data obtained from the first type of sample. The observed streaking fluctuates slightly, but maintains a similar qualitative behavior over most of the positions in the HAZ at one side of the sample axis corresponding to a similar direction of thermal gradient. The magnitude and the direction of the streaking changes with the location of the probed in the HAZ [Figs. 5(a)–5(f)]. The observed streaking fluctuates slightly but maintains a similar qualitative behavior over most of the positions in the HAZ on one side of the sample axis. To the left of the center of the sample axis the predominant slip system has Burgers vector $\mathbf{b}=\frac{1}{2}[011]$ and dislocation line along $\boldsymbol{\tau}=[2\bar{1}\bar{1}]$ [Figs. 5(a) and 5(b)]. At the position exactly on the sample axis the direction of thermal stresses coincides with [001]. For this direction the condition for multiple slip is fulfilled, and multiple slip systems are observed in the experimental Laue image and the streak is broadened in several directions [Fig. 5(c)]. On the opposite side, the predominant activated slip system changes and has Burgers vector $\mathbf{b}=\frac{1}{2}[011]$ and dislocation line along $\boldsymbol{\tau}=[21\bar{1}]$ [Figs. 5(d) and 5(e)]. At the position most remote from the central axis [Fig. 5(f)] the above slip system with $\mathbf{b}=\frac{1}{2}[011]$, $\boldsymbol{\tau}=[21\bar{1}]$ is accompanied by several more slip systems resulting in local rotations around $[\bar{1}10]$ and [110] directions. Most of the streaks split into several spots indicating dislocation grouping walls and the formation of geometrically necessary boundaries. The average misorientation angle through the boundary is equal to 0.2–0.4°.

Downloaded 04 Sep 2009 to 160.91.157.167. Redistribution subject to AIP license or copyright; see http://jap.aip.org/jap/copyright.jsp

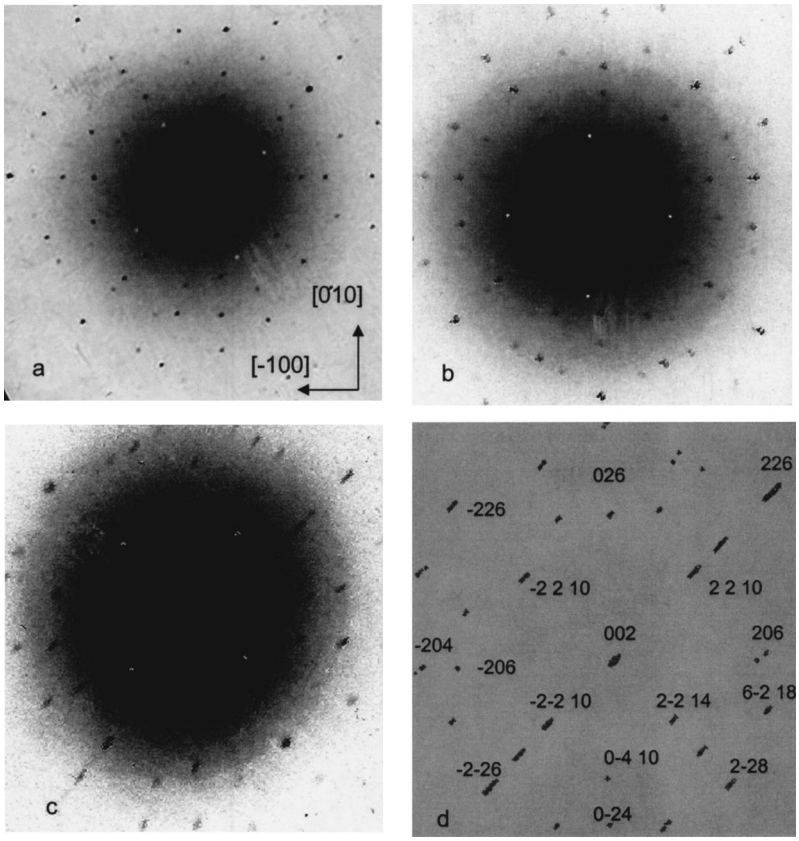

FIG. 3. Laue diffraction from the first sample type: (a) from fusion zone; (b) from base material; (c) within the HAZ but only 100 μm from the FL; (d) simulated Laue image with slip geometry corresponding to dislocation with Burgers vector $\mathbf{b}=[110]$, $\boldsymbol{\tau}=[1\bar{1}2]$ if $\mathbf{b}=[110]$, $\boldsymbol{\tau}=[1\bar{1}\bar{2}]$.

C. Electron microscopy of the HAZ

The microstructure of the BM of the single crystal, far from the HAZ is shown in Fig. 6(a). This structure is typical for nickel-based superalloys after thermal treatment. It contains cuboidal particles of γ' phase equally distributed in the γ matrix of the alloy. The average size of the particles is equal to 650 nm and their volume fraction was calculated to be 74%. The microstructure of the HAZ differs considerably from the BM structure. In our experiments only approximate positions of the regions in the HAZ are specified since their exact position relative to FL could not be determined in the TEM samples. Within the HAZ the large cuboidal γ'-phase particles partially dissolve. During cooling, small secondary γ'-phase particles are formed. The size distribution of the γ'-phase particles becomes bimodal [Figs. 6 and 7]. The average size of the newly formed particles is 50–70 nm. This value is seven to eight-times smaller than the size of the primary γ' particles [Figs. 6(a) and 6(b)]. The same size

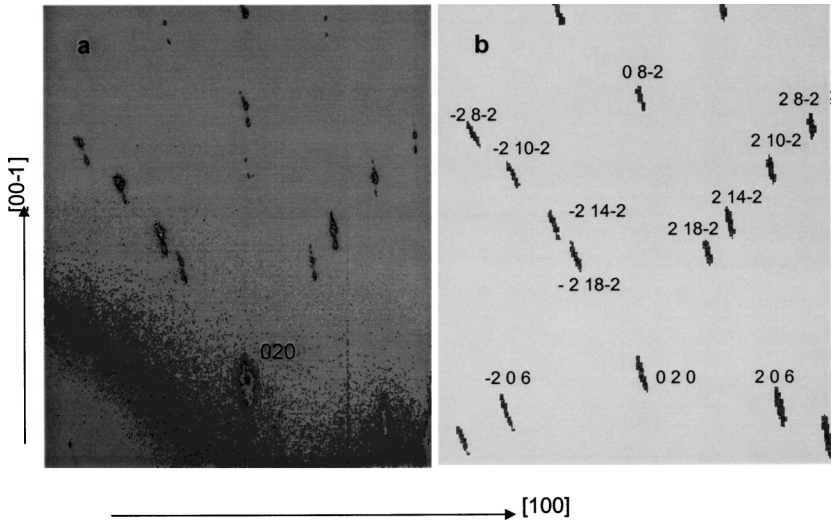

FIG. 4. (a) Laue images obtained with synchrotron microbeam Laue diffraction; (b) simulated Laue image with dislocation slip system $\mathbf{b}=[011]$, $\boldsymbol{\tau}=[21\bar{1}]$.

Downloaded 04 Sep 2009 to 160.91.157.167. Redistribution subject to AIP license or copyright; see http://jap.aip.org/jap/copyright.jsp

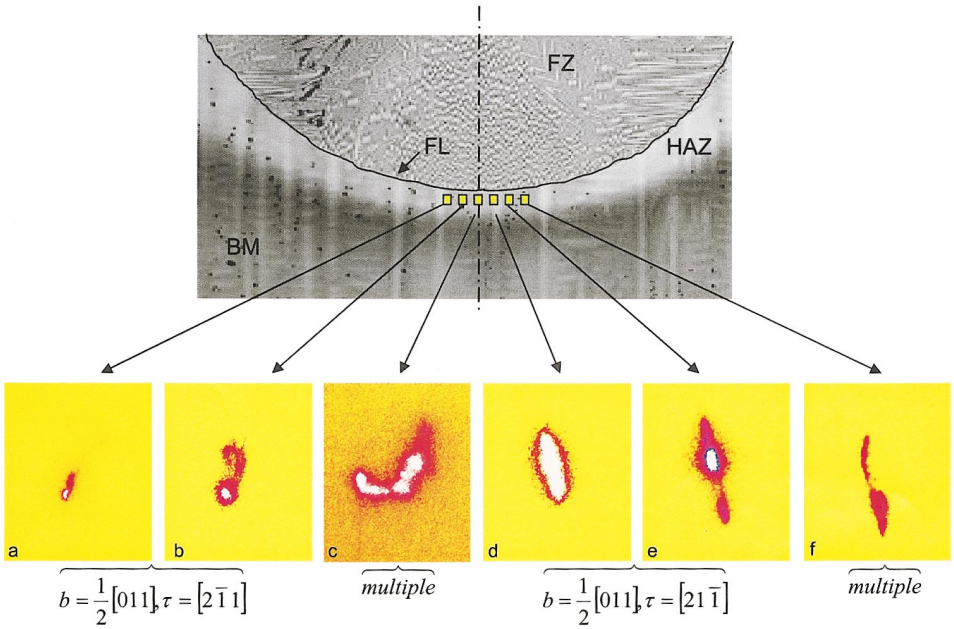

FIG. 5. Location of analyzed points relative to FL and sample axis (upper part) and (002) Laue reflection from synchrotron microdiffraction obtained from the HAZ (100 μm from FL) and different distances from the sample axis: (a) 200 μm to the left; (b) 100 μm to the left; (c) at the sample axis, multiple slip; (d) 100 μm to the right; (e) 200 μm to the right; (f) 300 μm to the right.

distribution is typical for nickel-based superalloys after one stage high temperature aging.[10] The closer one gets to the FL, the higher the temperature this location reaches during welding. That is why the process of dissolution of large primary γ' phase particles is more complete [Figs. 6(a) and 6(c)]. The bimodal nature of γ' particles observed in Fig. 6(b) can be interpreted as following. During heating to high temperatures the primary γ' particles dissolve. The dissolution of γ' leads to increased activity of dislocations along the $\{111\}$ planes in the γ' phase as the sample cools from high temperature. These mobile dislocations interact with each other to form sessile dislocations. With further cooling, the second wave of γ' precipitates form which leads to the bimodal distribution of γ' in the final microstructure interspersed with dislocation networks. Close to the FL γ'-phase particles dissolve completely. As a result, in this region of the weld only small secondary γ' phase particles are observed [Fig. 6(d)]. In the regions more distant from the FL but still within the HAZ, the volume fraction of large particles is equal to $\approx$66% [Fig. 6(b)].

The dislocation structure in the HAZ also changes significantly. In the BM, dislocations are absent [Fig. 6(a)], while dislocations appear in the HAZ. Their density is minimal far from the FL and it increases as one approaches the FL [Figs. 6(b), 7(b), and 7(c)]. It reaches a maximal value in the positions directly neighboring the FL [Fig. 6(d)]. The maximum number of dislocations is observed in the matrix of the single crystal between the large γ'-phase particles and near the γ/γ' interface boundary [Fig. 7(a)]. Dislocation lines having *Z*-shape lines are elongated along two directions mutually perpendicular to [100] and [010]. The dislocation types (**A** or **B**) are identified using different **g** operations (Table I). For edge dislocations $(\mathbf{g}\cdot\mathbf{b})=0$ and $\mathbf{g}(\mathbf{b}\times\boldsymbol{\tau})=0$ (where $\boldsymbol{\tau}$ is the edge dislocation line unit vector) and $(\mathbf{g}\cdot\mathbf{b})=0$ for screw dislocations. They correspond to dislocations **A**

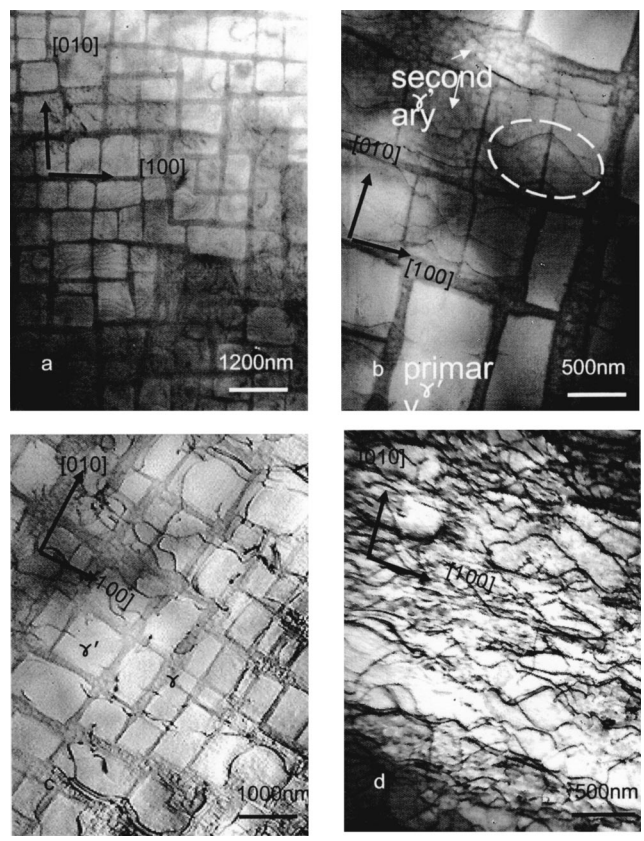

FIG. 6. Morphology of γ'-phase and dislocation structure within (a) the base material, and (b), (c), (d) HAZ; (a) Volume fraction of γ'-phase is $\sim$0.74; Dislocations are not observed. (b) HAZ closest to base material: Partial dissolution of large primary γ'-phase particle and subsequent precipitation of fine γ'-phase during cooling. The circled region shows the "zig-zag" nature of dislocation networks. (c) In the middle of the HAZ: partial dissolution of the γ'-phase and the number of dislocations also increase. (d) In the HAZ close to FL: complete dissolution of the γ'-phase and formation of dislocation network with zigzag dislocations.

Downloaded 04 Sep 2009 to 160.91.157.167. Redistribution subject to AIP license or copyright; see http://jap.aip.org/jap/copyright.jsp

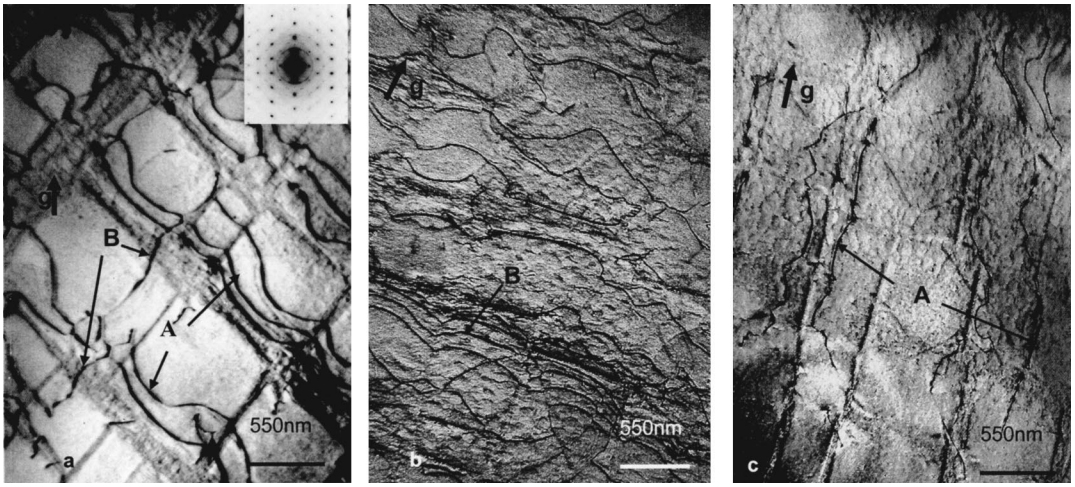

FIG. 7. Dislocation structure within the HAZ of the TSM75 single crystal, close to the FL. **A**- zigzag dislocations along the average direction [100] with Burgers vector parallel to **b**=[101]; **B**—zigzag dislocations along the average direction [010] with Burgers vector parallel to **b**=[011]; (a) Dislocation distribution along the γ/γ' boundaries; Both **A** and **B** type dislocation sets are visible; **g**=(220); Beam direction is close to (001); (b) Dislocation network in the γ matrix formed by **B**-type dislocations is visible; **g**=(020); Beam direction is close to (001); (c) Dislocation network in the γ matrix formed by two A-type dislocations is visible; **g**=(200); Beam direction is close to (012).

and **B** in Fig. 7, with Burgers vectors [101] and [011], respectively. The elongation of the *Z*-shaped segments parallel to the $\langle 100 \rangle$ direction indicates a Lomer-Cottrell type of dislocation reaction [showed with dashed oval in Fig. 6(b)].

IV. DISCUSSION

A transition from one dislocation network to another is observed in the weld [Figs. 5(a)–5(f)]. Correlated fluctuations in streaking are observed in regularly spaced slip bands. Different dislocation patterns form because dislocations screen each other's stress fields.

The elements of the dislocation density tensor at each location in the HAZ can be written as

$$\rho_{ik} = \tau_i b_k \delta(r). \tag{1}$$

Here ρ_{ik} gives the sum of the dislocations whose Burgers vector b_k and line direction τ_i are parallel to k and axes i $(k,i=1,2,3)$, respectively. Following the approach[11,12] in the framework of strain gradient plasticity, the total density tensor ρ_{ij} of geometrically necessary dislocations which accommodate the distribution of thermal stresses relates to the strain gradient tensor η_{lmk} with the following equation:

$$\varepsilon_{ilm}\eta_{lmk} = -\rho_{ik}, \tag{2}$$

where $\varepsilon_{\tau lm}$ is the antisymmetric Levi-Civita permutation tensor ($\varepsilon_{123}=\varepsilon_{231}=\varepsilon_{312}=1$; $\varepsilon_{213}=\varepsilon_{132}=\varepsilon_{321}=-1$; and all other $\varepsilon_{ijk}=0$). Under multiple slip the intensity distribution around each reciprocal lattice point depends on the aforementioned dislocation density tensor and the effective strain gradient. η_{lmk} is the gradient of plastic distortion tensor η_{lm} in the x_k direction. Streak direction ξ of the Laue spot in that case depends on the directions of eigenvectors of the dislocation density and effective strain gradient tensors. Due to screening of thermal stresses, one slip system is overtaken by another slip system which leads to the complicated hierarchical dislocation structure in the HAZ near the FL of the spot weld. The density of dislocations ρ that leads to stress relaxation is roughly proportional to the variation of the temperature gradient $\delta\nabla T$, lattice parameter a, and thermal expansion coefficient, α,

$$\rho = \alpha\delta\nabla T/a. \tag{3}$$

The overall deformation behavior is highly correlated with the crystallographic orientation of the location in the HAZ and to the thermal gradients. On average, it results in lattice misorientations in the HAZ primarily around the axis perpendicular to the thermal gradient.

From the modeling of thermal parameters in the HAZ we know that the thermal gradient is perpendicular to the FL and the rate of its decrease is maximal in the narrow region near the FL. In the center of the sample it is parallel to the [001] direction along the *Z* axis (Fig. 1). Previously[2] we found that under such conditions eight possible slip systems may be activated with slip directions parallel to $[10\bar{1}]$, [011], [101], or $[01\bar{1}]$. When multiple slip is possible in the γ' matrix, dislocations accumulate on the γ/γ' interface. Several dislocation reactions are possible. The following Lomer-Cottrell type reaction between the partials,

$$\frac{a}{6}[121] + \frac{a}{6}[\overline{211}] \rightarrow \frac{a}{6}[\bar{1}10], \tag{4}$$

results in the Burgers vector along the interface and perpendicular to the direction of the dislocation line. Such partials were found experimentally. This forms an edge misfit dislocation at the interface. It has two trailing partials.[13–18] Similar reaction between other possible partial dislocations re-

TABLE I. Visibility-invisibility of different dislocation sets (vis: visible; inv: invisible).

Dislocation	**g**=(200)	**g**=$(2\bar{2}0)$	**g**=(020)	**g**=(220)	**g**=$(\bar{1}11)$	**b**
A	vis	vis	inv	vis	inv	(101)
B	inv	vis	vis	vis	vis	(011)

Downloaded 04 Sep 2009 to 160.91.157.167. Redistribution subject to AIP license or copyright; see http://jap.aip.org/jap/copyright.jsp

sults in the formation of a dislocation network in the γ matrix which covers the γ/γ' interface.

V. CONCLUSIONS

Microstructure transformations in the HAZ of the Ni-based single crystal have been characterized in detail using several tools, and the results include the following points.

(1) Dissolution of the γ' - phase particles during heating and secondary precipitation of γ' during cooling is found, as well as formation and multiplication of dislocations. This process is more intense as one approaches the FL. In the regions immediately neighboring the FL, γ' - phase particles dissolve completely and reprecipitate from the solid solution in the form of very small (10–20 nm) particles.

(2) In the immediate vicinity of the FL, the temperature gradient and the rate of its change reaches maximal values and causes the formation of large amounts of dislocations. Dislocations are concentrated in the γ' matrix of the single crystal superalloy.

(3) X-ray Laue diffraction (both conventional and microbeam) and electron microscopy show that alternating dislocations slip systems dominate in the HAZ with Burgers vector $\boldsymbol{b}=[110]$ and dislocation lines $\boldsymbol{\tau}_1=[1\bar{1}2]$ and $\boldsymbol{\tau}_2=[11\bar{2}]$; or $\boldsymbol{b}=[\bar{1}10]$, dislocation lines $\boldsymbol{\tau}_3=[112]$, and $\boldsymbol{\tau}_4=[11\bar{2}]$. Each of these two dislocation groups forms two *Z*-shaped dislocation lines fluctuating around two cubic directions [100] and [010].

ACKNOWLEDGMENTS

The research was sponsored by the Division of Materials Sciences and Engineering, Office of Basic Energy Sciences, US Department of Energy, under Contract No. DE-AC05-00OR22725 with UT-Battelle, LLC. The authors thank Dr. H. Harada of National Institute of Materials Sciences, Tsukuba, Japan for providing the samples used in the analysis.

[1] D. Dye, O. Hunziker, S. M. Roberts, and R. C. Reed, Metall. Mater. Trans. A **32**, 1713 (2001).
[2] O. Barabash, S. Babu, S. David, J. Vitek, and R. Barabash, J. Appl. Phys. **93**, 738 (2003).
[3] J.-W. Park, J. M. Vitek, S. S. Babu, and S. A. David, Sci. Technol. Weld. Joining. **9** (1), 1 (2004).
[4] B. C. Larson, W. Yang, G. E. Ice, J. D. Budai, and J. Z. Tischler, Nature (London) **415**, 887 (2002).
[5] R. Barabash, G. E. Ice, and F. Walker, J. Appl. Phys. **93**, 1457 (2003).
[6] ABAQUS, ver. 6.3-1, HKS (2003).
[7] J. Goldak, A. Chakravarti, and M. Bibby, Metall. Trans. B **15**, 299 (1984).
[8] B. Sundman, B. Jansson, and J.-O. Andersson, CALPHAD: Comput. Coupling Phase Diagrams Thermochem. **9**, 153-190 (1985).
[9] N. Saunders, Ni-DATA, v. 5, ThermoTech Ltd., Surrey Technology Centre, 40 Occam Road, Guildford GU2 5YH, United Kingdom (2001).
[10] R. E. Shalin, I. L. Svetlov, E. B. Kachanov, V. N. Toloranya, and O. S. Gavrilin, *Single Crystals of Nickel Based Superalloys*, (Metallurgy, Moscow, 1997), p. 336, in Russian.
[11] H. Gao, Y. Huang, W. D. Nix, and J. W. Hutchinson, J. Mech. Phys. Solids **47**, 1239 (1999).
[12] Y. Huang, H. Gao, W. Nix, and J. Hutchinson, J. Mech. Phys. Solids **48**, 99 (2002).
[13] H. Mughrabi, Acta Metall. **31**, 1367 (1983).
[14] T. Ohashi, K. Hidaka, and M. Saito, Mater. Sci. Eng., A **238**, 42 (1997).
[15] T. Ohashi, K. Hidaka, and S. Imaho, Acta Mater. **45**, 1801 (1997).
[16] J. X. Zhang, T. Murakumo, Y. Koizumi, T. Kobayashi, and H. Harada, Acta Mater. **51**, 5073 (2003).
[17] B. von Grossman, H. Biermann, U. Tetzlaff, F. Pyczak, and H. Mughrabi, Scr. Mater. **43**, 859 (2000).
[18] Z. P. Luo, Z. T. Wu, and D. J. Miller, Mater. Sci. Eng., A **354**, 358 (2003).

Downloaded 04 Sep 2009 to 160.91.157.167. Redistribution subject to AIP license or copyright; see http://jap.aip.org/jap/copyright.jsp